Growth and magnetism of Fe nanostructures on W(001)

W. Wulfhekel, F. Zavaliche, R. Hertel, S. Bodea, G. Steierl, G. Liu, and J. Kirschner
Max-Planck Institut für Mikrostrukturphysik, Weinberg 2, D-06120 Halle, Germany

H. P. Oepen
Institut für Angewandte Physik, Universität Hamburg, Jungiusstr. 11, D-20355 Hamburg, Germany
(Received 23 March 2003; published 13 October 2003)

We present a combined study of the growth, structure, and related magnetic properties of Fe/W(001) using low-energy electron diffraction, scanning tunneling microscopy, the magneto-optic Kerr effect, and scanning electron microscopy with polarization analysis. Different growth regimes arise due to a competition between the stress-related elastic energy and diffusion barriers. By increasing the growth temperature, diffusion mechanisms may be switched on, activating more and more diffusion paths that lead to a reduction of the elastic energy stored in the growing films. This results in strong variations of the structure and morphology of the films. The influence of each structural and morphological phase of the Fe films on the magnetic properties can be observed and is interpreted within micromagnetic theory.

DOI: 10.1103/PhysRevB.68.144416 PACS number(s): 85.75.−d, 68.37.−d, 75.70.−i

I. INTRODUCTION

The magnetic properties of ultrathin films are strongly influenced by interactions with the substrate via elastic energies.[1–3] The films are strongly bound to the substrate such that they adopt the lattice constant and structure of the substrate. The macroscopic misfit between film and substrate and the substrate's crystal structure induces a variety of different modifications[4–9] and morphologies[10] of the growing film. Most prominently, the magnetic anisotropy is influenced directly by the structure and morphology[11–13] and indirectly by the strain via the magnetoelastic coupling.[14–18] In the case of Fe on W(001) the misfit is 10.4%. This large a misfit causes elastic energies in a pseudomorphic film that are of the same order as the diffusion barriers of the relevant diffusion processes occurring during growth of the Fe film. Hence, during growth the competition between elastic energies and diffusion barriers results in a wide variety of growth structures. Depending on the growth temperature, some of the diffusion mechanisms may be frozen in and hence do not compete with elastic energies while at higher temperatures they are active. The different growth structures of the Fe film, however, vary in their magnetic properties. Hence, a detailed understanding of the interplay of diffusion mechanisms and the elastic energy is important to tailor the magnetic properties of ultrathin films.[18] In this study, we intend to illuminate this interplay and its impact on the magnetic properties of Fe films on W(001).

Fe on W(001) is a system that has been studied by several groups in the past.[18–29] Fe was found to grow pseudomorphically for the first few monolayers[18,19,23] despite the huge misfit with the substrate. The first two monolayers form a wetting layer[18,19,23] that is stable upon annealing up to 700 K.[19] For higher coverage, three-dimensional growth has been reported and annealing leads to islands on top of a two-monolayer Fe carpet.[10,18,23] The pseudomorphic bilayer shows a Curie temperature of $\approx$240 K,[23] while the monolayer is nonmagnetic.[23,30] There are conflicting reports on the magnetic easy axis. While some authors[21] report an easy axis along $\langle 110 \rangle$, others[24] report an easy axis parallel to that of bulk iron: i.e., $\langle 100 \rangle$. Magnetoelastic properties of Fe on W(001) were studied by Sander and co-workers[28,29] showing that at the immense strain the magnetoelastic energies also contain large terms of second order in strain. Further, few-monolayer-thick films show a strong deviation from the bulk magnetoelastic properties of Fe.

II. EXPERIMENT

All experiments were carried out in ultrahigh vacuum (UHV) at a base pressure of 5×10^{-11} mbar. The W(001) sample was cleaned by cycles of glowing in O_2 ($\approx$1700 K, 10^{-7} mbar) and flashing to $\approx$2500 K in the absence of O_2 until no contaminations were detected by Auger electron spectroscopy (AES) and low-energy electron diffraction (LEED) showed sharp (1×1) diffraction patterns with the absence of any superstructure. Scanning tunneling microscopy (STM) images revealed clean, flat terraces of sizes larger than 100 nm separated by single atomic steps. After cleaning of the W(001) surface, Fe (99.999% purity) was deposited by electron beam evaporation with a rate of $\approx$2 ML/sec. AES spectra of the deposited films showed no contamination, especially no C peak within the sensitivity limit of our spectrometer. Fe coverages were calibrated in pseudomorphic monolayers (ML) using STM and medium energy electron diffraction intensity oscillations. During growth, the sample was heated to different temperatures measured with a thermocouple attached to the sample holder in close vicinity of the sample. Other films were deposited at room temperature followed by controlled annealing. After film preparation, *in situ* characterization of the structure, morphology, and magnetism was carried out by LEED, STM, and the longitudinal magneto-optic Kerr effect (MOKE), respectively, at room temperature or below. Scanning electron microscopy with polarization analysis (SEMPA) was used in some cases to image the magnetization configuration of the Fe films. For this, the films were prepared and then transferred from the MOKE-STM chamber to a SEMPA chamber via a vacuum suitcase.[31]

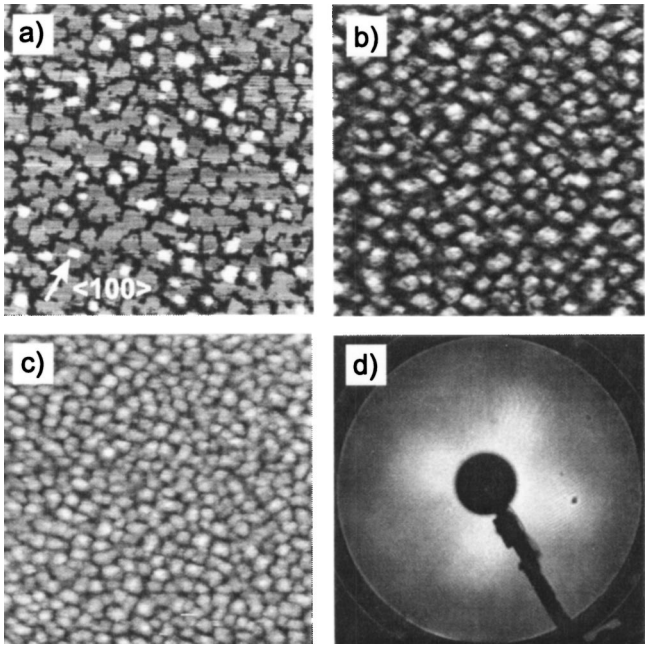

FIG. 1. STM images after deposition of (a) ≈2 ML, (b) ≈4.7 ML, and (c) ≈8.6 ML of Fe at 300 K. All images are 100 ×100 nm wide. (d) shows the LEED pattern of ≈8.7 ML of Fe at 125 eV. The first-order diffraction spots appear strongly blurred.

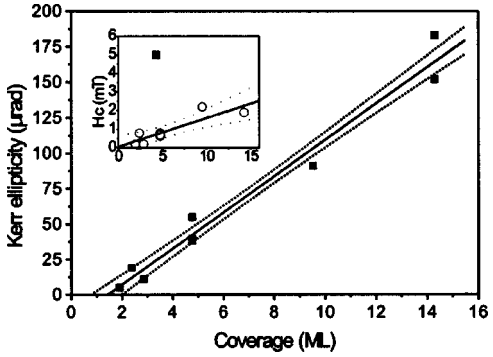

FIG. 2. Kerr ellipticity at remanence of Fe films of different Fe coverage with a linear fit and the 1σ expectation range. For films below 2.4 ML, the measuring temperature was 160 K while for the others 300 K. The inset shows the coercivity as a function of the Fe coverage for 300 K growth (open circles) and 400 K (solid squares).

III. RESULTS AND DISCUSSION

First, we concentrate on the limiting regimes of growth: i.e., low-temperature growth, where the film morphology is determined by the absence of strong diffusion, and high temperatures, where the film morphology reflects the thermodynamic equilibrium structure.

A. Film growth at room temperature

At room temperature, a low mobility of the deposited adatoms is expected. At 300 K, the deposited material arranges in small (≈10 nm), three-dimensional islands [see Fig. 1(a)]. The islands are irregular. Nevertheless, the symmetry of the W substrate is preserved and steps preferentially evolve along ⟨100⟩ directions. This indicates that the lateral diffusion of Fe atoms on W(100) is rather restricted at this temperature, leading to a high density of islands. Edge diffusion of atoms is still effective at 300 K, resulting in straight step edges. With increasing film thickness, the film roughens [see Figs. 1(b) and 1(c)]. Films of 8.6 ML coverage display up to six open atomic layers. This indicates an insufficient downward mass transport of atoms that are deposited on growing islands leading to the roughening of the films. Downward mass transport is strongly hampered. Hence, the structure of the film is in this case determined by the short diffusion length and the absence of interlayer mass transport.[32] LEED images [see Fig. 1(d)] show a blurred (1×1) structure for all energies—i.e., even for in-phase scattering conditions. For scattering conditions other than in phase, the blurred LEED pattern may be induced by the roughness of the film. At in-phase scattering conditions, however, LEED does not reveal any information on the layer distribution but only on the lateral position of atoms. Therefore, the strongly blurred LEED pattern indicates that in this case not all atoms are positioned on regular lattice positions of the W substrate. Possibly, the lattice of the higher layers laterally relaxes towards the bulk lattice constant of Fe in a partly elastic way, similar to Ge clusters on Si(001).[33] Additionally, strain relaxation by introduction of misfit dislocations gradually sets in around 3 ML total coverage as stress measurements revealed.[28,29] This leads to a displacement of the Fe atoms from the regular W lattice sites, as well. For such blurred LEED spots, however, the dislocations are expected to be rather unordered. Since at low growth temperatures the film morphology is governed by the growth kinetics, the strain in the film is largely determined by growth kinetics, too.

B. Magnetic properties of room-temperature-grown films

The magnetic properties of the films were studied taking magnetization loops with the MOKE at 300 K and 160 K for Fe coverages above and below 2.4 ML, respectively. Above a coverage of ≈1.6 ML, magnetic hysteresis loops could be observed at 160 K, while a coverage exceeding ≈2.3 ML was needed, to obtain a loop at 300 K. This finding is in agreement with former observations.[23] Figure 2 shows the measured Kerr ellipticity as a function of coverage. The measured data can be fitted well with a linear function, reflecting a constant volume magnetization of the film. The line, however, does not cross the origin but has a positive intersect with the abscissa. At coverages below this abscissa, we observed no magnetic signal at 160 K in agreement with Elmers and Hauschild.[23] Under the assumption that every atomic layer of Fe contributes to the ellipticity with the same constant, this observation can be interpreted as a lack of magnetization of the film either at the surface of the film or the interface to the substrate. Within the experimental error, the signal of one ML of Fe is missing (1.5±0.3 ML). This interpretation is supported by theoretical predictions that show a quenching of the magnetic moment of the first ML of Fe on W(001) at 0 K[30] or a reduced magnetic moment at the interface.[34] The magnetization loops for all thicknesses of Fe

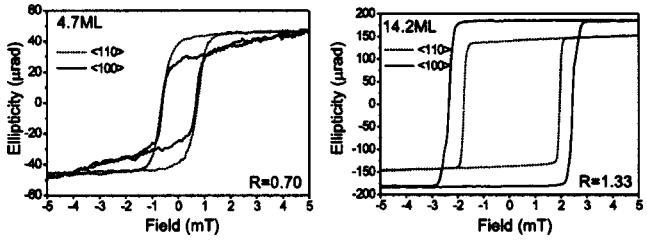

FIG. 3. Longitudinal MOKE magnetization loops of two films of thickness as indicated along ⟨100⟩ and ⟨110⟩ directions. The easy axis flips from the ⟨110⟩ direction in thin films to the ⟨100⟩ direction in films above ≈6 ML.

are rather square, especially for the thicker films (see Fig. 3). The coercivities of several mT are small (see the inset of Fig. 2), which is characteristic for an easy nucleation and propagation of domain walls. The well-defined switching between saturated states at the coercive fields suggests that only one or few domain walls are involved within the spot of the laser (1 mm). Interestingly, the easy axis of magnetization in the films of fourfold symmetry switches from the ⟨110⟩ direction in thin films to the ⟨100⟩ direction—i.e., the easy axis of bulk Fe—in thicker films. This can be deduced from the lower remanences observed in the hard-axis loops and the steady and reversible slope of the ellipticity beyond the coercivity, indicative of rotation processes. Since the system has fourfold symmetry, the easy axis and hard axis enclose an angle of 45°. At remanence along the easy axis, the full saturation magnetization is observed. When measuring the remanence along the hard axis, however, the magnetization points along an easy axis and only the projection of the magnetization along the measuring axis is seen. Due to the geometry, this is only $1/\sqrt{2}$ of the full remanence. Hence, in a fourfold system with homogeneous magnetization, the ratio R of remanences observed along ⟨100⟩ and ⟨110⟩ is either around 0.7 or 1.4. Within the experimental precision of typically 10%, these ratios are found (see Fig. 3). Hence, the films indeed may be described as homogeneously magnetized within the sensing spot of the laser. The flipping of the easy axis can be attributed to a fourfold anisotropy in thin films that favors a magnetization along ⟨110⟩, while in thick films, the bulk anisotropy dominates and rotates the easy axis along ⟨100⟩. The flipping is not caused by a transition of the films morphology and the resulting shape anisotropy, as for all thicknesses, island structures with edges along ⟨100⟩ directions are observed [see Figs. 1(a)–1(c)]. The observed anisotropy also reveals that despite the rather blurred LEED pattern, magnetically the Fe film is not disordered.

C. Growth at high temperatures and the thermodynamic equilibrium

In the other limiting case—i.e., in the case of growth at high temperatures—many diffusion mechanisms are active, allowing the deposited material to explore phase space to find the thermodynamically most favorite state. In accordance with the literature[10,19,23] we find the formation of three-dimensional islands on a 2 ML thick pseudomorphic carpet of Fe.[18] Growth proceeds in the Stranski-Krastanov

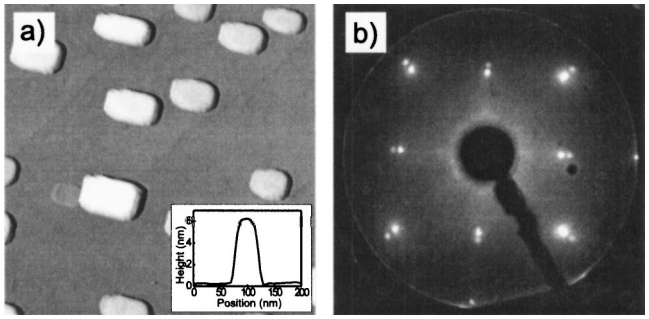

FIG. 4. (a) Slightly differentiated STM image of an Fe film of ≈4.7 ML after growth at 300 K and annealing to 800 K (300 ×300 nm^2). The inset shows a line profile across a typical island. (b) LEED diffraction pattern of the same film taken at 96 eV.

mode [see Fig. 4(a)]. Small Fe crystallites terminated by ⟨100⟩ steps are formed after growth or after annealing over 800 K. With STM we estimate that the equivalent of 2 ML Fe is missing in the volume of the crystallites and has to be present as a pseudomorphic carpet. Figure 4(b) shows the LEED diffraction pattern of an island film. Clearly, two sets of fourfold symmetric spots are visible: one corresponding to the lattice constant of W(001) and a weaker one of a ≈9% smaller lattice constant. This indicates that the islands are practically completely relaxed within the accuracy of our LEED (1% of the Brillouin zone). This also explains why they are themodynamically stable with their thickness of around 6 nm [see line profile in Fig. 4(a)]. Pseudomorphic Fe islands would not be stable due to the enormous strain energy of ≈300 meV per atom when taking the elastic constants of bulk Fe. Hence, in the case of high growth temperatures, strain relaxation mechanisms determine the film morphology. This scenario is contrary to the case of low-temperature deposition.

D. Magnetic properties of high-temperature-grown films

Magnetically, the Fe islands behave as independent small magnetic particles at 300 K, since the 2 ML carpet of Fe is not ferromagnetic at that temperature. Indeed, the MOKE hysteresis loops differ strongly from that of the low-temperature films. The loops are rounded (see Fig. 5), of s

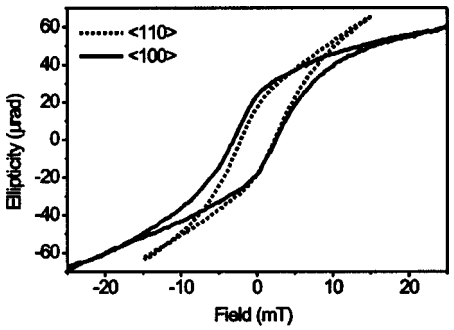

FIG. 5. Longitudinal MOKE loops along ⟨100⟩ and ⟨110⟩ directions of an Fe film of ≈4.7 ML after growth at 300 K and annealing to 800 K. The loops are minor loops. The films could not be saturated within the available magnetic fields.

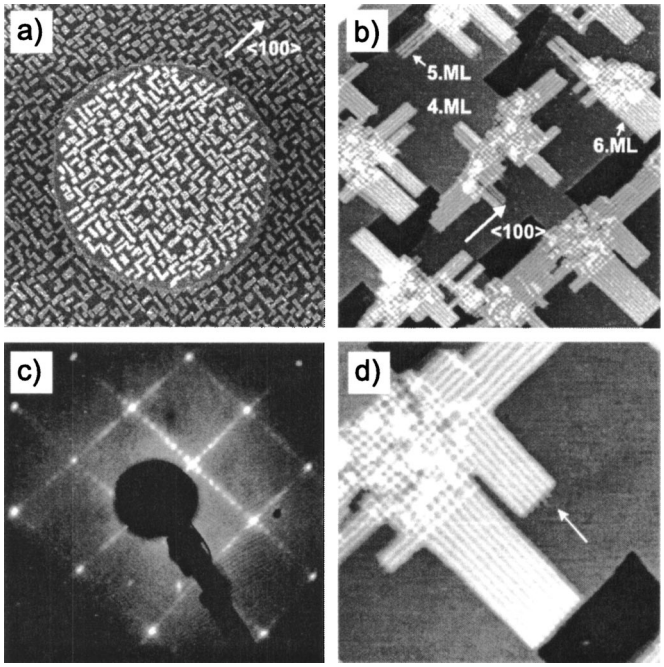

FIG. 6. STM images of Fe films after growth at 400 K (a) $\approx$2.3 ML (500×500 nm^2), (b) $\approx$4.3 ML (200×200 nm^2), and (d) $\approx$4.3 ML (100×100 nm^2). (c) LEED pattern of $\approx$4.7 ML Fe deposited at 400 K taken at 166 eV.

shape, and not saturated. We could not saturate the films within the available magnetic fields up to 35 mT. Hence, the observed loops represent minor loops. The coercivity of the minor loops, however, is much larger than that of the full loop of the continuous films. The s-shaped loops resemble the hysteresis loops of a set of Stoner-Wohlfarth particles with random orientation of easy axes.[35] With an average lateral extension of $\approx$50 nm and height of $\approx$6 nm, the islands are below the single-domain limit.[36,37] Due to their randomly elongated shape, the islands are expected to have different magnetic easy axes. This, in combination with their size distribution, leads to a distribution of switching fields which reflects in the s-shaped macroscopic hysteresis loop. More details on the single-domain behavior are discussed in Ref. 37. In summary, the film morphology is determined by the minimization of strain energy at high growth temperatures. As a result, small islands are formed that are below the single-domain limit and magnetically behave similarly to an ensemble of Stoner-Wolfarth particles.

E. Partial strain relaxation

After having discussed the limiting regimes of growth, we now concentrate on different intermediate growth temperatures. For both extreme cases—low- and high-temperature growth—three-dimensional structures evolve either due to kinetic effects or strain minimization. At intermediate temperatures between 400 and 500 K, however, STM reveals layer-by-layer growth [see, e.g., Fig. 6(a)]. At $\approx$400 K the mobility of the deposited atoms is sufficient to form flat and regular islands with step edges along $\langle 100\rangle$ or to attach to preexisting step edges [see round step edge in Fig. 6(a)]. Downward interlayer mass transport is active and two-dimensional growth is kinetically favored. Step edge diffusion is active as well, leading to the formation of compact and rectangular islands. Interestingly, sharp (1×1) LEED patterns (not shown) are observed up to 4 ML coverage, indicating the growth of pseudomorphic, fully strained Fe films. Strain relaxation in this system is much delayed in comparison to Fe/W(110), where dislocation formation already sets in around 1.5 ML.[38,39] In Fe/W(110) the film plane is a glide plane of bulk bcc Fe.[40] Thus in-plane strain can be easily released by a simple glide in the plane. For Fe/W(001), however, the film plane is not a glide plane of bulk Fe (Ref. 40) and the strain can only be released by gliding under an angle with respect to the film plane. This is kinetically hindered also because closed dislocation loops may not be formed.

When the coverage exceeds 4 ML, the kinetic barrier is overcome and dislocation lines running along $\langle 100\rangle$ directions are spontaneously formed, as seen in Figs. 6(b) and 6(d). The strain relief in the film is incomplete as it takes place underneath fifth- and sixth-layer islands, exclusively. In addition, a large fraction of these islands display only uniaxial strain relief by bundles of parallel dislocations.[18] This is further confirmed by the occurrence of a two-domain (9×1) LEED pattern [see Fig. 6(c)] caused by the parallel dislocation lines with a periodicity of nine lattice constants. The spontaneous formation of dislocation lines in the fifth ML also occurs when a fraction of a ML is deposited at 300 K on top of a 4-ML film grown at 400 K. The small fifth-layer islands display dislocations (not shown). This indicates that, with a coverage of 5 ML, a pseudomorphic arrangement of atoms is unstable at 300 K on time scales of the STM investigations (10 min). Interestingly, the fifth-layer islands display an elongated shape. The long axis lies along the dislocation lines—i.e., the fully strained direction [see Fig. 6(b)]. The islands therefore are fully strained along the long axis while the strain is relaxed along the short axis. This orientation does not reflect the thermodynamic equilibrium. It would be more favorable to extend the islands along their relaxed axes, since along the nonrelaxed axis the strain energy can only be saved by a slight elastic inward relaxation at the step edges. As the islands are not in their equilibrium shape, their shape is dictated by growth kinetics. It can be concluded that it is harder to nucleate a dislocation than to prolong an existing one. By this, dislocations in fifth-layer islands are created and travel like zippers through the film. The tensile strain is relieved and additional Fe atoms are incorporated into the film at the end of the dislocations, where the strain energy shows a local minimum. The islands expand along the dislocation line. Perpendicular to this, the islands also expand by incorporation of adatoms, but only to the width of about nine atoms. Wider islands are only observed when they contain more than one dislocation line. This effect also manifests in the fact that most islands have a width which is a multiple of the typical dislocation line separation of nine lattice constants. The depth down to which the dislocations extend into the Fe film is difficult to measure with STM. Figure 6(d) shows a higher-resolution STM image of an island with dislocations. As indicated by the arrow,

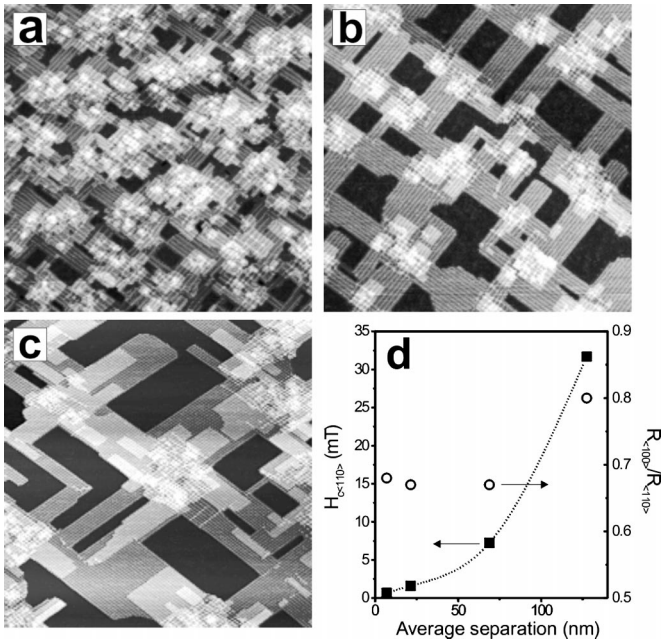

FIG. 7. STM images (a)–(c) of ≈4.7 ML Fe films on W(100) deposited between ≈360 and ≈440 K (200×200 nm^2). (d) Coercivities along ⟨110⟩ (squares) and ratio of remanences along ⟨100⟩ and ⟨110⟩ (circles) of ≈4.7 ML films as a function of the average separation of the dislocation bundles.

one can observe that the dislocation lines of the higher layer island continue in the fourth ML. Therefore dislocations at least reach down to the fourth layer. When comparing the height difference between the fourth biaxially strained Fe layer and a dislocated island of the sixth layer with the height difference between the second and fourth pseudomorphic layers, one obtains a $6\%\pm1\%$ larger height in the first case. Taking the bulk Poisson ratio of Fe $\nu=0.29$, one expects an expansion of the interlayer lattice constant of 4% upon an uniaxial relief of the 10% strain. Assuming that the Poisson ratio in thin and highly strained Fe films is similar to that in bulk Fe, the measured expansion indicates that the dislocations penetrate the fourth and possibly the third layer.

F. Dislocation bundles and magnetoelastic coupling

Magnetically, the Fe films with dislocation bundles behave strongly different from Fe films grown at 300 K, as has been discussed previously.[18] Here, we give only a condensed discussion that is necessary in the context of this paper. The inset of Fig. 2 shows that the coercivities of the 300 K films are in the range of 1–2 mT for thicknesses between 2 and 15 ML (open circles), while the film of 4.3 ML with dislocation bundles (solid square) displays a much higher coercive field. The increase of coercivity upon formation of dislocation bundles is significant, as the coercivity lies outside the 1σ band of a linear fit to the coercivities of the films grown at 300 K. Additionally, the MOKE loops of films with dislocations are not as square as the 300 K films.[18] This can be explained by an impeding of the domain wall motion due to dislocations.[18] Since dislocation formation at temperatures around 400 K exclusively takes place underneath fifth-layer islands, one may use the self-organizational effect of nucleation of the fifth-layer islands to vary the average separation between dislocation bundles. By increasing the growth temperature in the layer-by-layer growth regime slightly, the density of fifth-layer islands can be decreased in a wide range due to an exponential dependence of the island density on temperature.[41] As a consequence, the pattern size of the dislocation bundles—i.e., the average distance between dislocation bundles—can be tuned as shown in Figs. 7(a)–7(c). When measuring the coercivities as a function of the average separation, one observes a steep increase around 75 nm [see Fig. 7(d)]. For pattern sizes larger than 150 nm, we could not saturate the films with the available fields. Since the total number of dislocations varies only slightly in the different films, individual dislocations are ruled out to be responsible for the increased coercivities. However, the observed relation between coercivity and average separation hints at a micromagnetic explanation. The dislocation bundles are patches of high uniaxial strain. The strain is practically fully relaxed in the direction perpendicular to the dislocations while the full strain of ≈10% is still present along the dislocation lines. This enormous uniaxial strain ϵ induces a local uniaxial in-plane magnetic anisotropy $K_u\approx100$ kJ/m^3 via the magnetoelastic coupling of first and second order.[18,28] When a domain wall travels across a bundle of dislocations, the size relation between the wall width and bundle is of importance. An estimate of the width δ of a 90° Néel walls in the thin Fe films is given by $\delta=4\sqrt{A/K}\approx75$ nm, when the bulk exchange A (Ref. 42) and measured values for K (Ref. 18) are taken. If the average separation is smaller than δ, the exchange averages over the different local anisotropies and domain wall motion is hindered only little. Coercivities show only a small increase. However, if the average separation is larger than δ, the domain walls are influenced by the local variation of the anisotropy in the dislocation bundles and deform. Domain wall motion is impeded. Qualitatively, this explains the observed strong rise in the coercivities around 75 nm. Besides the influence of dislocation bundles on coercivity—i.e., a macroscopic property—measurements of the remanences along ⟨100⟩ and ⟨110⟩ as a function of the average separation indicate deviations from the simple single domain state. As can be seen from Fig. 7(d), below ≈75 nm the ratio of the remanences is $\approx1/\sqrt{2}$, which is caused by a fourfold magnetic anisotropy favoring the magnetization along ⟨110⟩ directions. A ratio of $1/\sqrt{2}$ of the remanences along hard and easy directions is a necessary condition for a fourfold system with homogeneous magnetization. However, when the size of the pattern is larger, the ratio significantly deviates from the geometric value. Hence, one can conclude that the magnetization is nonuniform across the film. It has been shown by micromagnetic calculations[18] that the direction of magnetization locally follows the modulated anisotropies causing magnetic in-plane structures in the 100 nm range. However, when the size of the pattern is reduced below 50 nm, the exchange prevents large deviations from the single-domain state and the local anisotropies are not reflected in the magnetic structure.[18] Hand in hand with the

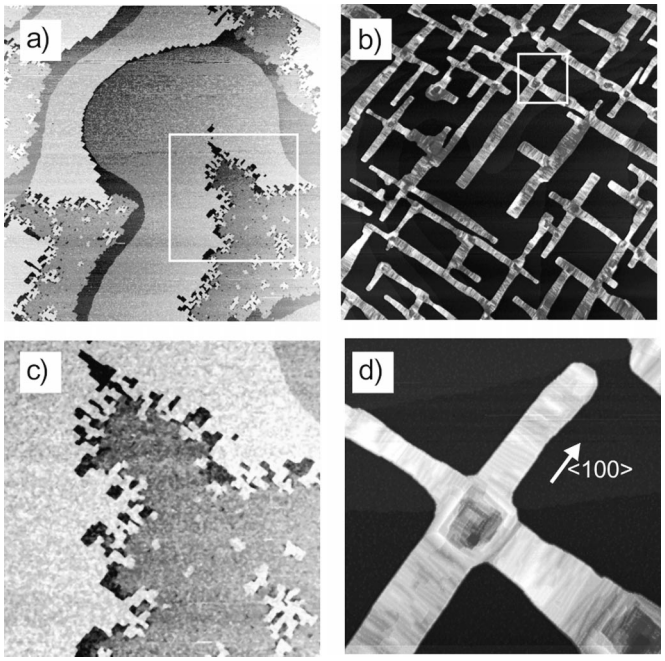

FIG. 8. STM images of ≈3.8 ML (a), (c) and ≈4.7 ML (b), (d) Fe on W(100) deposited at ≈500 K. Sizes in nm (a) 1000×1000, (b) 1500×1500, (c) 400×400, and (d) 300×300. (c) and (d) are zoomed in images as indicated in (a) and (b) by white frames.

appearance of the domains, also the coercivity increases for the micromagnetically calculated films,[43] in agreement with experiment.

G. Ostwald ripening and the formation cross-shaped nanostructures

The growth kinetics at 400 and 500 K differ significantly. At 400 K, areas with dislocations continuously grow with coverage in excess to 4 ML. The areas of the film with a local thickness of less than 5 ML remain in the (1×1) structure. At 500 K, however, the adatom mobility is higher and detachment of atoms from existing islands becomes feasible on the time scales of the growth. This results in two-dimensional Ostwald ripening; i.e., different areas of the surface are competing with each other via a two-dimensional adatom gas on the surface.[44] In this case, the dislocated areas attract material from the film and ''eat up'' the continuous carpet of 4 ML down to a coverage of 2 ML because the local binding energy is higher in the dislocated areas. This effect can be seen in Figs. 8(a) and 8(b). Below the critical coverage of dislocation formation, a continuous (1×1) Fe film is found with LEED and STM. Above that, the film splits up into dislocated, complex islands. The morphologies of the two films, however, are rather complex. For the films below 4 ML, the step edges and islands are not straight in spite of the high growth temperature. The step edges are ragged and islands show a dendritic shape [see Fig. 8(c)]. Since compact and rectangular islands are formed at lower growth temperatures [see, e.g., Fig. 6(a)], diffusion along the step edges has to be effective also at 500 K. This should result in square islands,[45] where the step edge energy is minimized. Therefore, at 500 K another mechanism has to override the minimization of step edge energy such that dendritic islands are stable in the presence of step edge diffusion. Interestingly, around the ramified step edges a surrounding depletion of 1–2 ML is often found [see Fig. 8(c)]; i.e., at the step edges the Fe film shows disruptions. This hints at a strain-driven mechanism. At step edges, the stress may be elastically relaxed without the formation of dislocations. As the strain-induced energies are of the order of 300 meV per atom (taking bulk Fe elastic properties), the energy gain by elastic relaxation may overcompensate the step edge formation energy, which is typically of the order of several 100 meV per atom.[46] By this, the length of the steps may be increased to save elastic strain energy.[47] This mechanism of forming dendrites is in sharp contrast to diffusion limited aggregates,[48] which form in the absence of step edge diffusion on hexagonal surfaces. Note that on square lattices dendritic island shapes have not been observed as, for the (100) surfaces, step edge diffusion is faster than adatom diffusion, always leading to compact islands even at low temperatures.[49] The morphology of the film completely changes when the coverage exceeds 4 ML. Dislocations are formed in the fifth ML and the 4 ML film is torn up into islands that are dislocated [see Fig. 8(d)] and 1–2 nm high (line profiles not shown). Interestingly, at these temperatures the long axis of the islands runs perpendicular to the dislocation lines which still occur in parallel bundles [see Fig. 8(d)]. This direction of elongation is in agreement with thermodynamic considerations reflecting the high adatom mobility. At some places, branches which run along perpendicular $\langle100\rangle$ directions may cross forming cross-shaped nanostructures. The width of the branches is around 50 nm. Magnetically, these structures are of interest, as they appear similar to the wiring on microelectronic circuits. In view of future applications in spin electronics with ferromagnetic leads, knowledge of the magnetic behavior of these self-organized pattern may be beneficial.

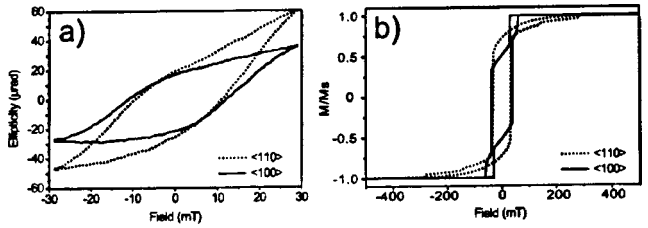

FIG. 9. (a) Longitudinal MOKE magnetization loops along $\langle100\rangle$ and $\langle110\rangle$ directions of an Fe film of ≈4.7 ML after growth at 500 K. The loops are minor loops and the films could not be saturated within the available magnetic fields. (b) Calculated magnetization loops of a cross-shaped island along $\langle100\rangle$ and $\langle110\rangle$ directions.

H. Magnetic properties of cross-shaped nanostructures

The macroscopic magnetic properties of the cross-shaped nanostructures were studied with the MOKE. The magnetization loops along $\langle100\rangle$ and $\langle110\rangle$ are shown in Fig. 9(a). Note that the loops are only minor loops, as the nanostruc-

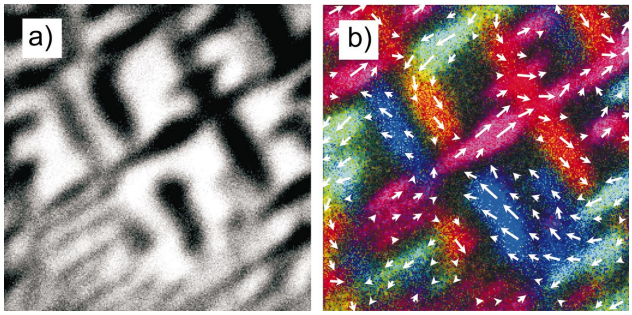

FIG. 10. (Color) SEMPA images of (a) the secondary electron yield and (b) the spin polarization of an ≈4.7 ML Fe film grown at 500 K. The vectors represent measured spin polarizations (direction and size) on top of the color-coded direction. Black represents a vanishing polarization. Sizes of the images are $1.5\times1.5\ \mu m^2$.

tured films could not be saturated with the available fields. The rounded loops indicate that the nanostructures are not behaving as a single-domain film. Although in continuous films of more than ≈7 ML we observe an easy axis along the ⟨100⟩ direction, a higher remanence and lower coercivity is found for thick islands along ⟨110⟩. This is even more surprising, as the elongated shape of the branches of the crosses also suggest an easy axis along ⟨100⟩. At first sight, the expected microscopic magnetic properties seem to differ from the experimentally observed macroscopic properties. This discrepancy, however, can easily be lifted with high-resolution SEMPA images of the magnetic structure of the crosses as displayed in Fig. 10. The Fe nanostructures were prepared and then transferred via a vacuum suitcase to the SEMPA chamber. Figure 10(a) shows a secondary electron image of the nanostructures. The crosses appear as dark stripes, as the secondary electron yield of the thick Fe structures is lower than that of the 2 ML thin pseudomorphic Fe film. In Fig. 10(b), the spin polarization of the secondary electrons is plotted, which is proportional to the sample magnetization.[50] First of all, the images taken at 300 K show a low or vanishing signal in between the islands (black areas). This is in agreement with the Curie temperature of the 2 ML carpet of ≈240 K. The islands, however, show a strong spin polarization. As has been deduced from the MOKE observations, the nanostructures are mostly not in a single-domain state. As one may expect from the shape anisotropy and the magnetocrystalline easy direction of bulk Fe, the magnetization follows the long axes of the branches running along ⟨100⟩ directions. At intersections or corners, the magnetization tries to curl such that a continuous flux is established [see vectors in Fig. 10(b)].

I. Micromagnetic simulations of cross-shaped nanostructures

To understand the experimental magnetization loops and remanences, we further performed micromagnetic simula-

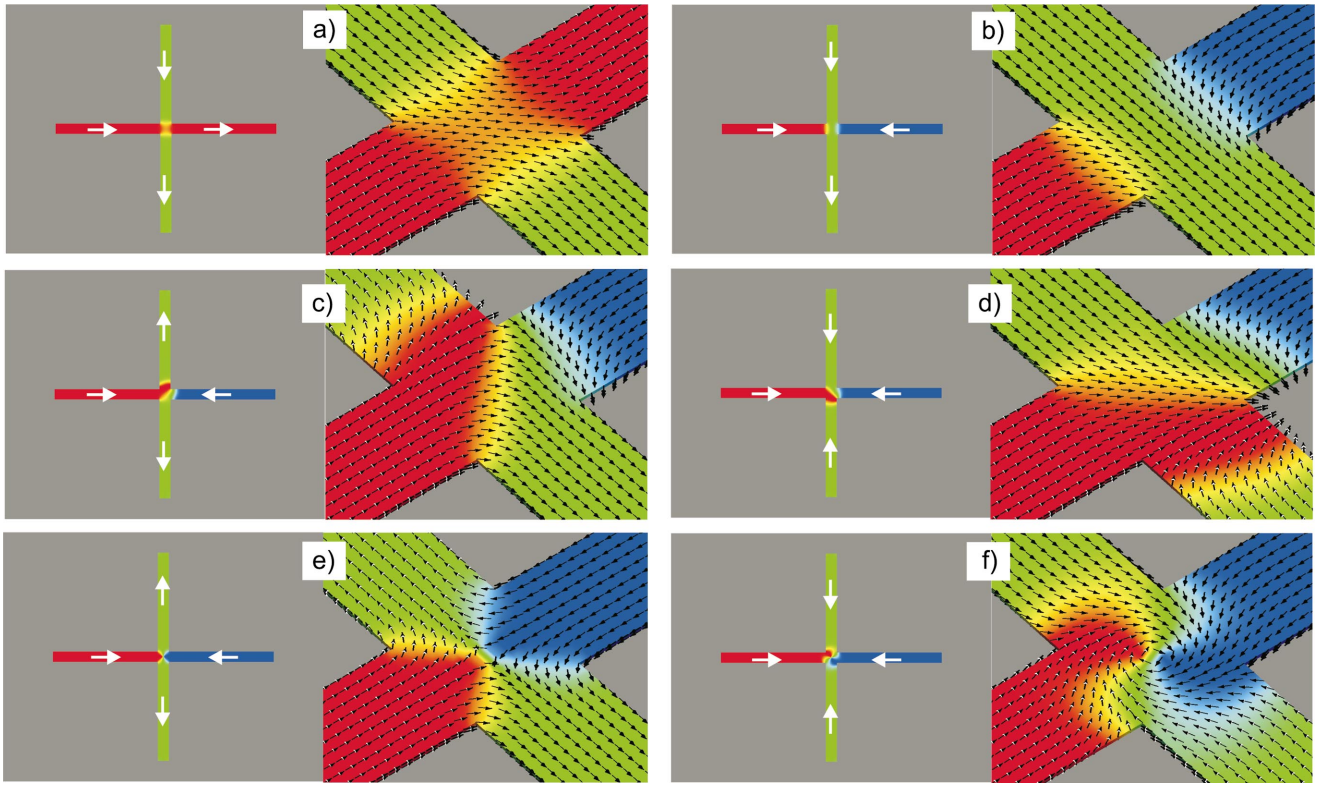

FIG. 11. (Color) Micromagnetic calculation of a cross of $1000\times1000\ nm^2$ size with arms of 50 nm width and 1.5 nm thickness. (a)–(d) are the ground-state configurations of the four principal magnetic configurations of the arms. (e) and (f) are high-energy states of the same principal configurations of the arms as (c) and (d). They contain an antivortex or a vortex in the crossing. The magnetization near the intersections is displayed in three-dimensional side views of higher magnification. The magnetization is encoded in color and is indicated by the vectors.

tions on the crosses and their magnetic switching with finite-element simulations. The model considered an Fe cross of two 1000 nm long and 50 nm wide strips. The thickness of the branches was 1.5 nm. The sample was discretized into $\approx 23\,800$ tetrahedral elements. Within the elements the magnetization profile was approximated by linear functions. Owing to the properties of the finite-element method, we locally increased the discretization density to increase the accuracy where it is required.[51] In the arms of the cross, the corner points of the elements are placed on a regular 5 nm grid, whereas in the intersection, the nodes of the elements are on a finer grid of 2 nm. The principle of the micromagnetic algorithm consists in minizing the total energy as a function of the orientation of the magnetization at each discretization point. The energy terms involved are Zeeman, stray field, anisotropy, and exchange energy. For the calculation of the anisotropy energy, the cubic magnetocrystalline anisotropy of Fe is considered up to the second nonvanishing order. The stray field energy is calculated by introducing a scalar potential U from which the stray field is derived as a gradient field $H = -\nabla U$. The potential U is the solution of Poisson's equation, which is solved by means of a hybrid finite-element and boundary-element scheme.[52] A more detailed description of the code is given in Ref. 53. The simulations show that only those configurations are stable in which the magnetization in the branches of the crosses lie along the branches. This is due to the shape anisotropy of the elongated arms and is in agreement with the SEMPA observations. This simple finding has strong consequences for the stable magnetic states of the cross. Every branch has only two possible directions of magnetization resulting in 2^4 states. The energy of these states does, however, not depend on the direction of the magnetization in the branches. It only depends on the relative direction of magnetization in the branches, as these determine the magnetic configuration at the intersection. Together with the rotational symmetry and mirror symmetry of the cross, the 2^4 states are reduced to four principal magnetic configurations that are depicted in Figs. 11(a)–11(d). For each of the four principal configurations of the branch magnetization, the ground state is displayed. The lowest-energy state of all four principal states is depicted in Fig. 11(a). The magnetization of the branches on opposite sides of the intersection is the same. At the intersection, the magnetization is rotated to the intermediate orientation in between that of the four arms. A 3% higher energy is found for the configuration shown in Fig. 11(b) where the magnetization of one pair of parallel branches continuously runs through the crossing while the magnetization of the other two branches is antiparallel to each other. In the latter branches, two 90° domain walls are formed at the intersection. An even higher energy displays the configuration depicted in Fig. 11(c). Here, both pairs of parallel branches are magnetized antiparallel. In one pair, the magnetization points towards the intersection, in the other away from it. For this principal configuration, two states are found with different magnetization patterns at the intersection. The lower state [see Fig. 11(c)] is by 76% higher in energy than the state of Fig. 11(a). One diagonal 90° domain wall is formed at the intersection and 90° domain walls in two of the branches. The other solution shown in Fig. 11(e) is 116% higher in energy than the lowest state. In this configuration, an antivortex with a singular point with perpendicular magnetization is found at the intersection, not unlike in cross tie walls.[54] This configuration, however, appears as an unstable equilibrium and eventually decays to the configuration displayed in Fig. 11(c) by a displacement of the antivortex to one of the corners of the crosses. Highest in energy is the configuration in which the magnetization of all branches point at or away from the intersection. Again, two possible states are found for this orientation of the magnetization in the branches. Figure 11(d) shows the lower one with 133% higher energy than the state of Fig. 11(a). At the intersection, a diagonal 90° wall is found and two branches contain 90° domain walls while the state of Fig. 11(f) is even higher in energy [225% higher than Fig. 11(a)] and shows a vortex in the center with a perpendicularly magnetized vortex core. Similar to the configuration of Fig. 11(e), this configuration eventually decays via vortex displacement into the lower state corresponding to Fig. 11(d). Also the configuration of Fig. 11(d) in ideal crosses does not appear to be stable. The configuration can lower its energy by expelling one or both 90° domain walls in the branches resulting in the states of Fig. 11(b) or 11(a). This transition may, however, be hindered by imperfections of the edges of the arms. In SEMPA images, only the low-energy states analogous to Figs. 11(a)–11(c) were found. The states represented by Figs. 11(d)–11(f) were never observed, in agreement with their much higher energies and the lack of stability.

Hysteresis loops were simulated for two different in-plane directions of the external field: parallel to an arm and along the diagonal, respectively. The field is swept in the range of ± 500 mT. The field step is generally 5 mT, but between ± 50 mT the field is changed in smaller steps of 1 mT after the converged solution is found. When applying an increasing magnetic filed along one of the arm axes, the branches parallel to the field may be switched easily (38 mT) while the magnetization in the other is continuously rotated away from the easy axis and can only be saturated at higher fields (60 mT). The corresponding hysteresis loop of this process is shown in Fig. 9(b). The remanence reflects only the magnetization of the branches that lie parallel to the measuring direction; i.e., in a statistical ensemble of many islands, it is $\frac{1}{2}$ of the saturation magnetization M_S. When, however, the magnetic field is applied under 45° to the branch axes, all branches switch at a field around 34 mT followed by a coherent rotation towards the field direction. The resulting hysteresis loop is depicted in Fig. 9(b). The remanence is higher, as all the branches contribute to it with the geometrical factor of $1/\sqrt{2}$. Therefore, the macroscopic loop shows a higher remanence than that along the branches, as seen in the experiment. The lower coercivity observed at 45° is explained by the easier nucleation of a domain wall at the end of the branches due to a higher torque. Hence, the macroscopic magnetic behavior as seen with the MOKE can be well explained by the behavior of the individual nanostructure.

IV. CONCLUSION

In this paper, we have discussed the intimate relation between the strain, film morphology, and magnetic properties.

A wide variety of structures in Fe films on W(100) were found. This variety is caused by a competition between strain energy and the energetic barriers for the relevant diffusion processes occurring during growth. With increasing temperature, more diffusion processes are allowed and the structure of the Fe film approaches the thermodynamic ground state. These different morphologies induce magnetic anisotropies either via magnetoelastic coupling or shape-dependent stray fields. This influence was detected in macroscopic hysteresis loops and in the magnetic configuration as seen with SEMPA. The findings were corroborated with finite-element micromagnetic calculations.

ACKNOWLEDGMENT

The authors acknowledge discussions with D. Sander.

[1] *Ultrathin Magnetic Structures*, edited by J.A.C. Bland and B. Heinrich (Springer-Verlag, Berlin, 1994), Vols. 1 and 2.
[2] M.T. Lin, J. Shen, W. Kuch, H. Jenniches, M. Klaua, C.M. Schneider, and J. Kirschner, Surf. Sci. **410**, 290 (1998).
[3] D. Sander, Rep. Prog. Phys. **62**, 809 (1999).
[4] G.A. Prinz, Phys. Rev. Lett. **54**, 1051 (1985).
[5] L. Gonzalez, R. Miranda, M. Salmeron, J.A. Verges, and F. Yndurain, Phys. Rev. B **24**, 3245 (1981).
[6] A. Clarke, G. Jennings, R.F. Willis, P.J. Rous, and J.B. Pendry, Surf. Sci. **187**, 327 (1987).
[7] C.M. Schneider, P. Bressler, P. Schuster, J. Kirschner, J.J. de Miguel, and R. Miranda, Phys. Rev. Lett. **64**, 1059 (1990).
[8] D. Renard and G. Nihoul, Philos. Mag. B **55**, 75 (1987).
[9] W. Wulfhekel, T. Gutjahr-Löser, F. Zavaliche, D. Sander, and J. Kirschner, Phys. Rev. B **64**, 144422 (2001).
[10] E. Bauer, Appl. Surf. Sci. **11-12**, 479 (1982).
[11] P. Krams, F. Lauks, R.L. Stamps, B. Hillebrands, and G. Güntherodt, Phys. Rev. Lett. **69**, 3674 (1992).
[12] A. Berger, U. Linke, and H.P. Oepen, Phys. Rev. Lett. **68**, 839 (1992).
[13] J. Chen and J. Erskine, Phys. Rev. Lett. **68**, 1212 (1992).
[14] U. Gradmann and J. Müller, Phys. Status Solidi **27**, 313 (1968).
[15] F. Huang, M.T. Kief, G.J. Mankey, and R.F. Willis, Phys. Rev. B **49**, 3962 (1994).
[16] W.L. O'Brien and B.P. Tonner, Phys. Rev. B **49**, 15 370 (1994).
[17] D. Sander, A. Enders, and J. Kirschner, J. Magn. Magn. Mater. **200**, 439 (1999).
[18] W. Wulfhekel, F. Zavaliche, F. Porrati, H.P. Oepen, and J. Kirschner, Europhys. Lett. **49**, 651 (2000).
[19] P.J. Berlowitz, J.W. He, and D.W. Goodman, Surf. Sci. **231**, 315 (1990).
[20] R.L. Fink, G.A. Mulhollan, A.B. Andrews, J.L. Erskine, and G.K. Walters, J. Appl. Phys. **69**, 4986 (1991).
[21] G.A. Mulhollan, R.L. Fink, J.L. Erskine, and G.K. Walters, Phys. Rev. B **43**, 13 645 (1991).
[22] J. Chen and J.L. Erskine, Phys. Rev. Lett. **68**, 1212 (1992).
[23] H.J. Elmers and J. Hauschild, Surf. Sci. **320**, 134 (1994).
[24] T.L. Jones and D. Venus, Surf. Sci. **302**, 126 (1994).
[25] M. Plihal, D.L. Mills, H.J. Elmers, and U. Gradmann, Phys. Rev. B **51**, 8193 (1995).
[26] H.J. Elmers, J. Hauschild, G.H. Liu, and U. Gradmann, J. Appl. Phys. **79**, 4984 (1996).
[27] H.J. Choi, Z.Q. Qiu, J. Pearson, J.S. Jiang, D. Li, and S.D. Bader, Phys. Rev. B **57**, R12 713 (1998).
[28] A. Enders, D. Sander, and J. Kirschner, J. Appl. Phys. **85**, 5279 (1999).
[29] D. Sander, A. Enders, and J. Kirschner, J. Magn. Magn. Mater. **198-199**, 519 (1999).
[30] R. Wu and A.J. Freeman, J. Magn. Magn. Mater. **127**, 327 (1993).
[31] W. Kuch, M. Salvietti, X. Gao, M.T. Lin, M. Klaua, J. Barthel, Ch.V. Mohan, and J. Kirschner, Phys. Rev. B **58**, 8556 (1998).
[32] G. Ehrlich and F. Hudda, J. Chem. Phys. **44**, 1039 (1966).
[33] Y.W. Mo, D.E. Savage, B.S. Swartzentruber, and M.G. Lagally, Phys. Rev. Lett. **65**, 1020 (1990).
[34] X. Qian and H. Hübner, Phys. Rev. B **67**, 184414 (2003).
[35] E.C. Stoner and E.P. Wohlfarth, Philos. Trans. R. Soc. London, Ser. A **240**, 599 (1948).
[36] R. Hertel, Z. Metallkd. **93**, 10 (2002).
[37] A. Yamasaki, W. Wulfhekel, R. Hertel, and J. Kirschner, Phys. Rev. Lett. **91**, 127201 (2003).
[38] U. Gradmann, M. Przybylski, H.J. Elmers, and G. Lui, Appl. Phys. A: Solids Surf. **49**, 563 (1989).
[39] D. Sander, R. Skomski, C. Schmidthals, A. Enders, and J. Kirschner, Phys. Rev. Lett. **77**, 2566 (1996).
[40] S. Amelinckx, in *Dislocations in Solids*, edited by F.R.N. Nabarro (North-Holland, Amsterdam, 1979), Vol. 2.
[41] J.A. Venables, Philos. Mag. **27**, 697 (1973).
[42] E. Kneller, *Ferromagnetismus* (Springer, Berlin, 1962).
[43] F. Porrati, Ph.D. thesis, University of Halle-Wittenberg, 2002.
[44] G. Rosenfeld, K. Morgenstern, I. Beckmann, W. Wulfhekel, E. Lægsgaard, F. Besenbacher, and G. Comsa, Surf. Sci. **402-404**, 401 (1998).
[45] G. Wulff, Z. Kristallogr. **34**, 449 (1901).
[46] P. Stoltze, J. Phys.: Condens. Matter **6**, 9495 (1994).
[47] H. Röder, K. Bromann, H. Brune, and K. Kern, Phys. Rev. Lett. **74**, 3217 (1995).
[48] H. Brune, Ch. Romainczyk, H. Röder, and K. Kern, Nature (London) **369**, 469 (1994).
[49] H. Brune, Surf. Sci. Rep. **31**, 121 (1998).
[50] J. Unguris, D.T. Pierce, A. Galys, and R.J. Celotta, Phys. Rev. Lett. **49**, 72 (1982).
[51] R. Hertel and H. Kronmüller, IEEE Trans. Magn. **34**, 3922 (1998).
[52] D.R. Fredkin and T.R. Koeler, IEEE Trans. Magn. **26**, 415 (1990).
[53] R. Hertel, J. Appl. Phys. **90**, 5752 (2001).
[54] E.E. Huber, Jr., D.O. Smith, and J.B. Goodenough, J. Appl. Phys. **29**, 294 (1958).